Received: 26 July 2020 | Revised: 14 September 2020 | Accepted: 28 October 2020

DOI: 10.1002/jemt.23641

RESEARCH ARTICLE

MICROSCOPY RESEARCH & TECHNIQUE WILEY

Rheological and tribological characterization of novel modified graphene/oil-based nanofluids using force microscopy

Mustafa Oguzhan Caglayan[1,2]

[1]Faculty of Engineering, Bioengineering Department, Bilecik Seyh Edebali University, Bilecik, Turkey

[2]Faculty of Engineering, Nanotechnology Department, Cumhuriyet University, Sivas, Turkey

Correspondence
Mustafa Oguzhan Caglayan, Faculty of Engineering, Bioengineering Department, Bilecik Seyh Edebali University, Bilecik, Turkey.
Email: caglayanmoguzhan@gmail.com, oguzhan.caglayan@bilecik.edu.tr

Funding information
Türkiye Bilimsel ve Teknolojik Araştirma Kurumu (The Scientific and Technological Research Council of Turkey), Grant/Award Number: 113M302

Review Editor: Alberto Diaspro

Abstract

In this study, it is aimed to improve the lubrication and anti-wear characteristics of nanofluids produced by the distribution of silane-modified graphene nanosheets into the base oil without any surfactant or dispersant. Nanofluids are among the hottest research topics currently studied in the literature due to their interesting thermal and rheological properties. Graphene nanosheet with unique physicochemical properties is a good alternative as a nanofluid component and a lubricant. In this study, the behavior of nanofluidic films on the material was investigated by using scanning probe techniques, phase-contrast microscopy, and friction force microscopy techniques. Due to stick–slip behavior and rheological properties that are dominant in the studied ranges, problems were encountered in performing tribological analyzes with friction force microscopy. On the other hand, these results have been beneficial in determining tribological factors in nanoscale. The presented nanofluids showed non-Newtonian behavior at high concentrations and shear rates and shown an improved tribological performance up to 43% in friction coefficient, 91% in wear, and 46% in thermal conductivity compared to the base oil.

KEYWORDS

friction force microscopy, graphene nanosheets, lubrication, micromechanical methods, nanofluids, phase-contrast microscopy

1 | INTRODUCTION

Nanofluids are among the hottest research topics currently studied in the literature with over 11,000 articles in the Scopus database in the last decade (Eswaraiah, Sankaranarayanan, & Ramaprabhu, 2011b). After the term nanofluidic was first introduced to the literature by Choi and Eastman (1995), nanofluids have been the strongest candidates to replace traditional working fluids in many industries with heating or cooling processes. This is because the thermal properties of nanofluids are more advanced than the traditional working fluids, and they may show non-Newtonian flow behavior (Yu, France, Routbort, & Choi, 2008). Friction is used or occurs as an active force in many physical processes, and also causes energy and material losses during these processes (Childs, 1983). The use of lubricants in these processes is the most effective method of eliminating friction-related undesired effects (Stachowiak & Batchelor, 2006). The additives also add features such as anticorrosion, abrasion resistance, and antioxidation in lubricating oils, and they function to increase lubricant performance, and lubricants containing certain amounts of nanoparticles are also nanofluids (Choi & Eastman, 1995). The high thermal and electrical conductivity and high load-carrying capacity of nanoparticles encourage the use of these nanomaterials in nanofluids (Peng, Chen, Kang, Chang, & Chang, 2010). Numerous studies have been carried out on the heat transfer properties of such nanofluids (He et al., 2007). Furthermore, various researchers have attempted to use nanomaterials to increase antifriction and anti-wear properties (Chen, Liu, & Yu, 1998). Antifriction and anti-wear behaviors depend on the characteristics of nanoparticles such as size, shape, and concentration (Wu, Tsui, & Liu, 2007). Phenomena such as colloidal effect, rolling effect, the protective film-forming effect, and the effect of the third

component in the matrix have been proposed as the mechanism of friction reduction and anti-wear behavior of nanoparticles in lubricants (Gara & Zou, 2013; Saidur, Leong, & Mohammed, 2011).

However, the development of nanoparticle-containing lubricants progresses relatively slow, because nanoparticles added to oil-based lubricants have the problem of forming agglomerate and losing stability due to their high surface energy (Yu & Xie, 2012; Zhao, Chen, & Ren, 2017). Since nanoparticle agglomeration and sedimentation diminishes the lubricant properties, adding dispersant into the nanofluid is a method that reduces the agglomeration and increases stability, but is often not preferred (Ghadimi, Saidur, & Metselaar, 2011).

Recently, the effect of particle size, morphology, and nanoparticle concentration has been studied to minimize friction and wear (Hwang et al., 2011; Reeves, Menezes, Lovell, & Jen, 2013). It has been reported by researchers that oil-based nanofluids obtained by adding TiO_2, SiO_2, Al_2O_3, Fe_2O_3, ZnO, CuO, CeO_2, $CaCO_3$, and ZrO_2 nanoparticles can reduce friction and reduce wear compared to a base oil (Choi et al., 2009; Gu, Li, Gu, & Zhu, 2008; Hernandez Battez et al., 2006; Hernández Battez et al., 2008; Hu & Dong, 1998; Hu, Dong, & Chen, 1998; Jiao, Zheng, Wang, Guan, & Cao, 2011; Kao & Lin, 2009; Wu et al., 2007; Yu et al., 2008; Yu, France, et al., 2008). It has been reported by different researchers that there is an approximately 30% decrease in both friction coefficients and the wear behavior when nanofluids are used (Gara & Zou, 2013; Gu et al., 2008; Zhang et al., 2011). It has also been reported that the tribological performance of ZnO, Al_2O_3, TiO_2, and MoS_2 nanoparticles in water-based nanofluids is high (Binggeli & Mate, 1994; Gao, Sun, Zhang, & Xue, 2000; Gara & Zou, 2012; Zhao et al., 2017).

The thermal properties of lubricating oils are also important. It was determined that the base oil with TiO_2 nanoparticle added reduced the friction coefficient and contact temperature (Chang, Zhang, Zhang, & Friedrich, 2005). It has been shown that the thermal conductivity of nanofluids incorporating low amounts of nanomaterials has increased (Baby & Ramaprabhu, 2010; Eastman, Choi, Li, Yu, & Thompson, 2001), for example, a 150% increase in thermal conductivity in nanofluids based on 1% multiwalled carbon nanotube-engine oil was reported (Choi, Zhang, Yu, Lockwood, & Grulke, 2001). The thermal properties improvements described by various physical mechanisms, such as the Brownian motion or the change in the distribution of liquid molecules at the particle/liquid interface, depending on the size, edge roughness, and amount of defects for graphene oxide (GO) (Kleinstreuer & Feng, 2011; Nika, Pokatilov, Askerov, & Balandin, 2009).

Due to its unique mechanical, electrical, physical, and thermal properties (Lee, Wei, Kysar, & Hone, 2008; Li, Xie, Li, Liu, & Li, 2011; Marconnet, Panzer, & Goodson, 2013; Novoselov et al., 2004), GO is used in many fields such as material engineering, energy, biotechnology, and electronics (Aravind, Baby, Arockiadoss, Rakhi, & Ramaprabhu, 2011; Bahadır & Sezgintürk, 2016; Chen et al., 2007; Eswaraiah, Sankaranarayanan, & Ramaprabhu, 2011a; Kumar et al., 2011; Li et al., 2011; Qu, Liu, Baek, & Dai, 2010). After the reduction of GO, most of the oxygen-containing groups present in GO, especially hydroxyl, epoxy, and carboxyl groups, are eliminated, and GO is converted to π-conjugation rich graphene, in other words, reduced GO (RGO) (Schniepp et al., 2006; Stankovich et al., 2007). While GO has a low conductivity and is a water-dispersible material, RGO has high conductivity and dispersion stability in water is low (Lotya, King, Khan, De, & Coleman, 2010; Park & Ruoff, 2009). Due to the dispersibility of graphene-based material is low, especially in oil-based nanofluids, for this reason, surface modification is required in the use of graphene in oil-based nanofluids, and various modification techniques have been developed to physically or chemically bond functional molecules onto graphene sheets (Stachowiak & Batchelor, 2006). In this study, graphene nanosheets (GNS) obtained by advanced oxidation of graphene was used as the main component.

The investigation of tribological behavior with the atomic force microscope (AFM) was carried out for the first time in the mid-1990s (Bhushan & Ruan, 1994). It is a delicate instrument that determines the van der Waals, electrostatic, and electronic interaction forces created between an ultrafine probe and the sample surface (Charrier & Thibaudau, 2005). Including the advantages of ultralow forces and high resolution under the working conditions, AFM is a tool that can be used in tribological characterization in this case where the capillary effects provided by the adhesion and absorbed water layer are very low in the contact between the tip and the sample (Bhushan & Ruan, 1994; Marti, 1993). AFM has been frequently used by researchers to determine the friction and wear properties of various coatings and lubricants (Liu & Bhushan, 2003; Moser & Eckhardt, 2001; Tambe & Bhushan, 2004; Tambe & Bhushan, 2005; Tambe & Bhushan, 2005a; Tambe & Bhushan, 2005b).

Phase-contrast microscopy (PCM), which is one of the measurement methods in noncontact mode AFM, takes advantage of the contrast in the viscoelastic properties (viscous energy dissipation) of different materials on the surface. A viscoelastic material flexes periodically when it is subjected to periodic stress. However, the stress response delays when an oscillating force is applied, because the viscoelastic material follows this oscillation with a phase shift in the frequency of the oscillation (Ahn, Chizhik, Dubravin, Kazachenko, & Popov, 2001). Phase angle contrast is a function of viscoelastic properties where extremely high vibration amplitude and low tip-to-sample distances are applied (Scott & Bhushan, 2003). PCM is proportional to the viscoelastic properties of the sample along with the attractive, repulsive, or adhesive forces at the interface (Anczykowski, Gotsmann, Fuchs, Cleveland, & Elings, 1999; James et al., 2001; Tamayo & García, 1997), but it is independent of the surface topography and elastic properties of the sample (Bar, Delineau, Brandsch, Bruch, & Whangbo, 1999; Binggeli & Mate, 1994).

With AFM, wear tests are performed by repeating a certain load range and determining the critical load at which the scars begin to occur (Bhushan, 2001). However, in this study, wear-test results could not be obtained with AFM since the device used could not form a wear scar on the Si surface. Another AFM-based method used in this study, friction force microscopy (FFM), is used to obtain topography and friction maps of surfaces, simultaneously (Bhushan & Ruan, 1994; Reinstädtler, Rabe, Goldade, Bhushan, & Arnold, 2005). In addition to

this method, the force modulation technique is used to obtain elasticity maps of soft surfaces (Maivald et al., 1991). It has been found that friction in nanosize depends on the normal load and sliding speed (Gnecco, Bennewitz, Pfeiffer, Socoliuc, & Meyer, 2004; Hsu & Chang, 2009; Tao & Bhushan, 2007).

In this study, tribological characterization was performed in oil-based nanofluids of GNS and derivatives with known anti-abrasion and antifriction properties. Also, a comprehensive rheological investigation of oil-based GNS derivative nanofluids was performed. Scanning probe techniques were used as micromechanical test methods. In this context, it was aimed to determine the viscoelastic behavior and friction coefficients of nanofluidic films on the material using techniques such as PCM and FFM with AFM. The high spatial resolution of AFM may make it possible to perform comparative tests in higher resolution and smaller areas compared to macro mechanical tests. However, as mentioned in the literature, these techniques have some difficulties. This study identified such problems and suggested solutions to problems where possible.

2 | EXPERIMENTAL METHOD

All chemicals used in this study are Sigma-Aldrich, Merck, or Alfa Aesar products, unless otherwise specified, analytical grade materials were used without additional purification. Unless otherwise stated, the results of all analyzes are given as the arithmetic mean and standard deviation of the data obtained by performing at least three repetitions. It is recommended that the reader refers to the Supplementary Document of this article for additional explanations on some topics.

2.1 | Production and modification of GNS

The modified Hummers method was used in the synthesis of GO (Hummers & Offeman, 1958; Wu et al., 2009). The GNS were subjected to advanced oxidation for the silane modification. The silane molecule binding processes for the modification of GNS are the condensation reaction carried out in the anhydrous environment. The modification was performed using 3-aminopropyl triethoxysilane (SilA), N-(6-amino hexyl) aminomethyl trimethoxysilane (SilB), and triethoxy (octyl) silane (SilC). While SilA and SilB were obtained using GNS, RGO was used for SilC production. RGO was obtained according to the method described by An Wong and Pumera (2014). Production of SilC-GNS started with the addition of 2% RGO by mass into 50 ml of toluene and sonication in an ultrasonic bath for 30 min. The dispersed RGO was taken into a three-necked flask, 0.5% by weight of SilC/toluene solution was added on it, and it was reacted at 70°C for 6 hr under the reflux. The product obtained at the end of the reaction was separated by centrifugation and washed several times with the toluene/methyl alcohol mixture to remove impurities.

Production of SilA-GNS and SilB-GNS was carried out under the same conditions. GNS was treated with oxygen plasma at 100 W for 10 min before modification. Oxygen plasma treatment was carried out using Diener (Germany) plasma device. GNS (2% by mass) was dispersed in 50 ml absolute ethyl alcohol in an ultrasonic bath for 30 min. Then, 10 ml of SilA and SilC solution (1% by mass) in absolute ethyl alcohol was taken and transferred into a three-necked flask containing GNS. The reaction was carried out under the reflux at 70°C for 6 hr. After the reaction was terminated, the product was obtained by washing with absolute ethyl alcohol and centrifugation.

2.2 | Transmission electron microscope, X-ray diffraction, Fourier transform infrared, X-ray photoelectron spectroscopy, and AFM characterizations

Transmission electron microscope (TEM) measurements of the materials were carried out at 200 kV using a JEOL 2100 HRTEM (JEOL, Japan) device. Samples were analyzed in dry and powder form. X-ray diffraction (XRD) analyzes were carried out using the Rikagu Miniflex X-ray diffractometer (Japan) with monochromatic Cu Kα radiation, 30 kV, and 15 mA operating voltage and current. Samples were scanned between 2θ 10–60° at 0.04° step size and 2°/min rate. The infrared spectra of the materials were taken with the Bruker Tensor 27 Fourier transform infrared (FTIR) spectrophotometer device using the KBr disk method in the range of 400–4,000 cm^{-1} wave number. X-ray photoelectron spectroscopy (XPS) analyzes were carried out with the device having an X-ray anode with AlKα monochromatic radiation (1,486.6 eV) operating on PHI 5000 Versa Probe model (ULVAC-PHI, Japan). The analysis samples were prepared on the glass substrate. Topography images of the materials were obtained by noncontact mode AFM (ParkSystem XE-100E) on Si (100) substrate. AFM images were obtained from an area of 1 μm × 1 μm–5 μm × 5 μm with 512-pixel resolution using NSC15 AFM-tips (at 317 kHz). The scan speed, z-servo gain, and setpoint were 0.75 Hz, 0.3, and 34 nm, respectively. Size analysis, including roughness analysis, was carried out using the device's XEI software. In the data given in the form of a table, the average and standard deviation of the measurements of at least five measurements were reported.

2.3 | Colloidal stability of nanofluids

The stability of the produced GNS, RGO, SilA-GNS, SilB-GNS, and SilC-GNS in an aqueous medium, absolute ethyl alcohol, and base oil was determined. Stability experiments were carried out against time by comparing the UV–vis spectra of GNS dispersed in different matrices using an ultrasonic bath in different ratios. During the studies, Shimadzu UV-2600 spectrophotometer (Japan) and quartz cuvettes were used. During the analysis, samples were taken from the vials kept at room temperature, from the middle of the bottle, and with a 5 ml micropipette. During the process, care was taken not to mix the sample in the container.

2.4 | Rheological measurements

Rheological measurements were carried out with Malvern Kinexus Pro (UK) model rheometer. Cone geometry with a 50 mm diameter and a 2° angle was used for rheological measurements. The distance between the cone and the nonrotating plate is taken as 0.05 mm.

2.5 | FFM, wear tests, and AFM calibration

In FFM tests, Si (100) substrate was used together with SiC tipped Si spring AFM probe. FFM analyzes were performed at different scanning speeds and various normal forces up to 300 nN. The FFM tests were carried out at 25°C using a table with a Peltier temperature control element. Si-wafer was used as a homogeneous surface substrate for calibration purposes (Bhushan & Ruan, 1994). For FFM analysis, the effects of surface topography on friction were minimized by performing scans in two directions (Ţălu, 2015). Also, the horizontal bending coefficient of the probe was determined by using a standard cantilever approach and applying axial sliding instead of the V-type cantilever approach in the method proposed by Ogletree, Carpick, and Salmeron (1996) and Ruan and Bhushan (1994). Also, it is necessary to know the shape of the AFM tip before and after use; however, since electron microscopy analysis is both time-consuming and costly, the shape of the AFM tip was estimated using calibration pattern and modeling using the method described elsewhere (Bhushan & Kwak, 2007b) (please refer to Supplementary Document for details of calibration). Wear tests were carried out in the longitudinal direction (perpendicular to the scan direction) of the cantilever by applying normal force up to 300 nN at certain and repetitive cycles (200 times) and a speed of 50 μm/s.

2.6 | Thermal conductivity tests

Thermal conductivity was measured with the device using the transient hot wire (THW) method (Decagon KD2 Pro). This method relies on the ASTM D2717 standard method and is described elsewhere (Peñas, Zárate, & Khayet, 2008). Nanofluids prepared in different concentrations for thermal conductivity measurements were brought to the measuring temperature between 30 and 60°C in 5°C steps without any mixing process after mixing in the ultrasonic bath. Measurements were made by repeating five times.

2.7 | PCM and tip calibration

The rheological properties of the produced nanofluids were examined by PCM. For this purpose, the noncontact mode measurement was performed using different scanning speeds and oscillation frequency around the natural oscillation frequencies of the AFM cantilever. The possible differences due to the height difference and the structure of the material were minimized using Si-wafer as a substrate. Using the calibration and modeling proposed by Scott and Bhushan, the obtained phase shift data was used for viscosity measurements (Scott & Bhushan, 2003). The adhesion hysteresis of the nanofluid was determined by repeated force spectrum measurements on a droplet in contact mode. During modeling, the conical AFM tip assumption was made, and the approximate dimensions were determined using the method reported by Bhushan and Kwak (2007a). In noncontact mode measurements, only the adhesion force was taken into account and the interaction of the AFM tip with the surface was neglected. Also, according to the area that interacts with the AFM tip, the nanofluid droplet was considered infinitely large. Thus, boundary effects were not included in the calculations. The mass of the AFM tip was estimated as no calibration was performed to detect tip mass (1×10^{-11} kg). The cantilever spring constant and other cantilever-related parameters of the probe were applied to the model according to the values in the certificate specified by the manufacturer for each batch (ParkSystem, Korea). In PCM experiments, noncontact mode AFM cantilevers were cleaned together with the cantilever holder using ethyl alcohol, nitrogen plasma cycle (at 100 W RF, 10 min.), and were used in the experiments as long as the natural oscillation frequency does not change.

2.8 | Ball-on-disc tribotester

The tribological behavior of the materials was investigated by using a ball-on-disc tribotester device (UTS Tribometer T10, Turkey). For this purpose, a modified tribometer was used to include a modified sample holder for lubricant measurements. Tests were carried out at constant rotation speed with loads of 1, 2, and 5 N determined according to the operating limits of the device. All experiments were carried out for 1,800 s (i.e., about 40 m sliding distance). During the experiment, surface temperature, depth of abrasion, friction force, and friction coefficients were recorded. Alumina balls (Ø = 6 mm, hardness H = 16.14 GPa, root-mean-square [RMS] roughness 250 nm) and commercial low alloy DIN 18CrMo4 steel (hardness H = 6.67 GPa, RMS roughness 253 nm) were used as friction pairs. Ambient humidity during the tests was between 30 and 40% (RH) and ambient temperature was between 21 and 24°C. Before friction and wear tests, steel plates and balls were cleaned in an ultrasonic bath using acetone, ethyl alcohol, and water, respectively. Since the depth of wear in the sample was measured with a tribometer, no additional measurement was performed.

3 | RESULTS AND DISCUSSION

3.1 | Characterization of produced nanomaterials

The diffraction peak for GO was obtained at 11.8° (2θ) and is compatible with the previously reported values (10–12.4°) (Lee, Ko, & Kim, 2012). The distance between the layers was calculated as 0.75 nm, and this value was higher than the graphite layer distance

given in the literature about 0.34 nm and showed that the graphite was oxidized. Two diffraction peaks were obtained for the SilA-GNS (12.0 and 6.1°) and the interlayer distance was calculated as 0.74 and 1.45 nm. Three separate diffraction peaks were obtained for the SilB-GNS (11.3, 7.1, and 5.8°), and the distances were 0.78, 1.24, and 1.52 nm, respectively. The third peak observed may have resulted from the binding of the silane molecule between the layers with a different orientation. Diffraction peaks for SilC-GNS were obtained at 14.2 and 7.3°, and the distance between layers corresponding to these peaks was 0.62 and 1.21 nm, respectively. The distance between layers of 0.62 nm is small compared to the 0.74 nm value obtained for GNS. Due to the absence of oxide groups and possibly bound water for RGO, the distance between layers is expected to be lower than GO. Furthermore, the increased inter-layer distance for all silane-modified GNS was shown that the molecules used in the modification increase the inter-layer distance as a result of intercalation. However, the layer distance observed in all silane-modified GNS around 0.7 nm indicated unmodified GNS in the structure.

The bands 3,350; 1,740; 1,626; 1,168; and 1,030 cm^{-1} of in the infrared spectrum of the oxidized GNS indicate functional groups containing oxygen. In particular, characteristic C═O (—COOH) at 1,740 cm^{-1} and —OH vibrations at 3,350 cm^{-1} confirm that GNS is synthesized. In addition, the C═O stretch at 1,626 cm^{-1}, and the bands of the C═O and C—O vibrations at 1,168 and 1,740 cm^{-1} are also characteristic for GNS. Around 950–1,050 cm^{-1}, there is a characteristic peak of C—O—C symmetrical stretching. After the reduction, the intensity of the characteristic C═O band belonging to the carboxylic and carbonyl group in the infrared spectrum of GO, and the bands at 1,740 cm^{-1}; 1,168; and 1,030 cm^{-1} indicating the oxygen-containing functional groups in GO decreased. The band obtained at 1,626 cm^{-1} has shifted to around 1,573 cm^{-1} and showed that the carboxylic or carbonyl groups of graphene are not reduced to C—OH. Also, C—O—C stretching band observed around 1,050 cm^{-1} has disappeared after reduction (Xu et al., 2015).

In the IR spectrum of SilC-GNS, —OH stretch at 3,410 cm^{-1} and C═O stretching band at 1,620 cm^{-1} were obtained. In addition, the peak intensity observed around 1,380 cm^{-1} (—OH vibration) decreased considerably but did not disappear. Two separate peaks around 2,920 and 2,840 cm^{-1} associated with methylene groups, and the Si—O band (quite small) observed around 790 cm^{-1} indicate that the SilC modification has taken place. However, it can be said that the SilC modification was realized as a result of FTIR analysis, but the amount of SilC bound on the RGO was relatively low. This small amount of silane attached to the GNS may be related to the use of RGO instead of GO. However, due to the reaction of triethoxy (octyl) silane should be carried out in toluene rather than absolute ethyl alcohol, and the difficulty arising in distributing GO into less polar toluene, RGO was required to be used. In the SilA-GNS and SilB-GNS IR spectra, —NH_2 observed at 1,642 cm^{-1} (together with —OH @ 1,620 cm^{-1}), —NH observed at 1,560 cm^{-1}, C—N observed around 1,210 cm^{-1}, Si—O bands observed around 1,050, 786, and 481 cm^{-1} shown that SilA and SilB modifications have successfully achieved.

In the XPS spectrum for SilA-GNS, 284.8 eV (C—C), 286.2 eV (C—O), 287.8 eV (C═O), and 289.0 C(O)O peaks overlapped and gave a high amplitude peak (Stankovich et al., 2007). When curve fitting is performed in the Si2p spectrum, the 100.2 eV peak found indicates the Si—C and the 101.3 eV peak indicates the Si—O bond. This is another result showing that the silane modification process has taken place. Besides, the peak obtained around 530 eV corresponds to the binding energy of the Si—O and C═O bonds (Xu, Yan, Cong, Zhu, & Li, 2017). Another peak is the peak observed at 408 eV of the N—H bond in the silane molecule used in the modification. The XPS spectrum for SilB-GNS and SilC-GNS turned out to be similar to the spectrum obtained for SilA-GNS, and due to the similarity in the molecules used for modification, their bond energies are approximately the same. While the characteristic peaks of Si—C at 99.8 eV and Si—O bonds at 100.8 eV were obtained for SilB, Si—C peaks at 100.4 eV and Si—O peaks at 100.9 were obtained for SilC. In addition, the peaks of the C bonds of GO gave a broad band cumulatively. Due to the NH and NH_2 bonds in the structure, around 400 eV N_{1s} peak was obtained.

Transparent characteristic morphology of GO can be seen in TEM images. In TEM images of silane-modified GNS, morphology is not very different from unmodified GO. It can be seen that the layers come together by folding more and form a dark contrast image. In addition, it was also observed in AFM images that the plates were folded more and their size decreased and the edge defects also increased relatively (Figure 1). In AFM images, lateral force images are given because the contrast is higher and the size and separation of graphene sheets can be chosen more clearly. Another remarkable point in these images is the accumulation caused by the agglomeration of graphene sheets, possibly due to their high surface energy, even after the excess diluted colloids are spread onto the surface for AFM measurements.

The average peak to valley roughness (R_{pv}) was obtained around 2.31 ± 0.08 nm and the RMS roughness was around 0.32 ± 0.03 nm for GNS. In the sample modified with SilA, R_{pv} has obtained around 2.21 ± 1.09 nm and the RMS roughness value was found around 0.33 ± 0.21 nm. The uncertainty of roughness measurements given as 2σ is higher than GNS due to the folded structure of the material. R_{pv} roughness was 6.43 ± 1.34 nm and 5.91 ± 0.96 nm, RMS roughness was around 1.24 ± 0.33 nm and 1.14 ± 0.29 nm, for SilB-GNS and SilC-GNS, respectively. The RMS roughness value was not fully compatible but was also noticeably close to the interlayer distance obtained from XRD data (approximately 0.3 nm).

3.2 | Colloidal stability of nanofluids

In the stability tests, the change of absorbance of GO, RGO, SilA-GNS, SilB-GNS, and SilC-GNS measured in the base oil against time was examined. The stability of SilA-GNS-base oil was higher compared to RGO. This difference is observed in all SilA-GNS concentrations, especially in 0.1% and 0.05% SilA-GNS concentrations. This may have been caused by the binding of silane groups added to the

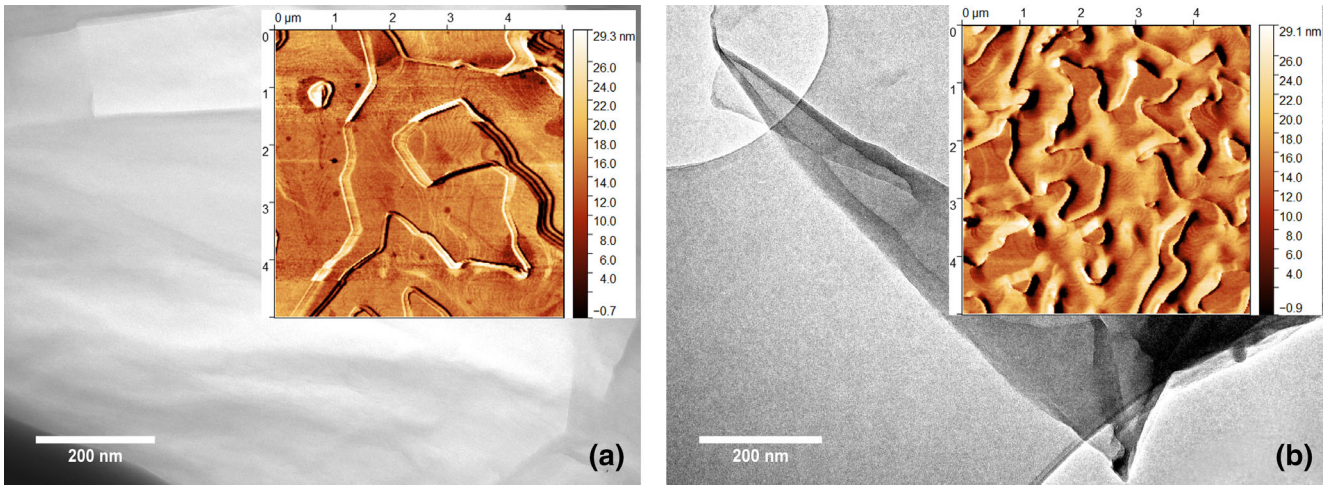

FIGURE 1 Transmission electron microscope (TEM) and atomic force microscope (AFM) images for graphene oxide (GO) (a), and modified graphene nanosheet (GNS) (b). Figures are representatives of produced nanomaterials, for demonstration purposes, AFM images presented here were lateral force microscopy data [Color figure can be viewed at wileyonlinelibrary.com]

structure to the existing O and OH groups. SilB-GNS and SilC-GNS had similar stability. It can be said that especially in high concentrations (e.g., 0.5%), rapid precipitation occurs in the first 24 hr, while in the concentration of 0.05% SilB and SilC-GNS, there is very little agglomeration and precipitation during 48 hr. In general, silane-modified GNSs produced in the study were found to be more stable than GO and RGO nanofluids of the same concentration, especially when the base oil nanofluid contained GNS at low concentration (e.g., ≤0.1% by weight).

3.3 | Rheological characterization

Rheological measurements of nanofluids containing SilA, SilB, and SilC were performed, and in Figure 2, shear stress and apparent viscosity versus shear rate graphs for oil-based nanofluid containing SilB-GNS are shown, respectively (at 25°C). The behavior of the nanofluid in the experimental range shifted slightly towards the non-Newtonian regime as the nanoparticle concentration in it increases.

The viscosity of SilB-GNS-base oil nanofluid was around 0.75 Pa. s for 0.05% (by weight) and about 2.1 Pa.s for 0.5% (by weight) nanofluid. The viscosity at lower shear rates was dependent on the shear rate for nanofluid containing 0.2 and 0.5% SilB-GNS. The change in the apparent viscosity of the nanofluids against shear rate was not significant at 25°C. However, in the study where temperature and apparent viscosity relationship were examined, especially at low temperatures, it was observed that the apparent viscosity changes with the shear rate. The non-Newtonian behavior was observed for these nanofluids prepared with >0.1% (by weight) SilA or SilC. The change of apparent viscosity at different temperatures was examined using a nanofluid containing 0.01% SilA, SilB, and SilC-GNS at a shear rate of about 20 s^{-1} at a temperature range of −20 to +40°C. The change between visible viscosities and temperature was modeled using the function of $\mu = Ae^{-T/t_o} + \mu_o$ and the parameters of this function are given in Table 1.

Non-Newtonian behavior observed at high concentrations at room temperature was observed in all silane-modified GO nanofluids at low temperatures. This behavior has become more dominant at temperatures lower than 0, −5, and −10°C for SilA-GNS, SilB-GNS, and SilC-GNS, respectively. Viscosity increased with added silane-modified GNS. As the GNS has a nanolevel structure, it was expected that the viscosity would decrease. However, the fact that GNS is agglomerated even at low concentrations and that the interaction between GNS and base oil is high even though agglomeration does not occur may have caused this situation. The pseudoplastic behavior observed in the base oil at low temperatures increased with the increase in the amount of modified GNS in the nanofluid. Also, as the temperature increases, the viscosity difference between base oil and nanofluid was reduced, possibly due to Brownian motion (He et al., 2007).

3.4 | Tribological tests with FFM and tribology maps

The friction maps (or friction contour maps) of the materials provide detailed information about the friction behavior (Tambe & Bhushan, 2005b). Friction due to slipping depends on operating conditions, material properties, environmental conditions, and interface characteristics (Tao & Bhushan, 2006). In Figure 3, a contour map of the friction forces obtained at various sliding speeds and various normal loads is given for the base oil nanofluid with added 0.1 and 0.5% silane-modified GNS by mass, respectively. According to Tambe and Bhushan, if the contour lines are in the form of horizontal lines, the friction force does not depend on the sliding speed (Tambe & Bhushan, 2008). If the contour lines are vertical, the friction force does not depend on the normal load. Contour lines with positive or

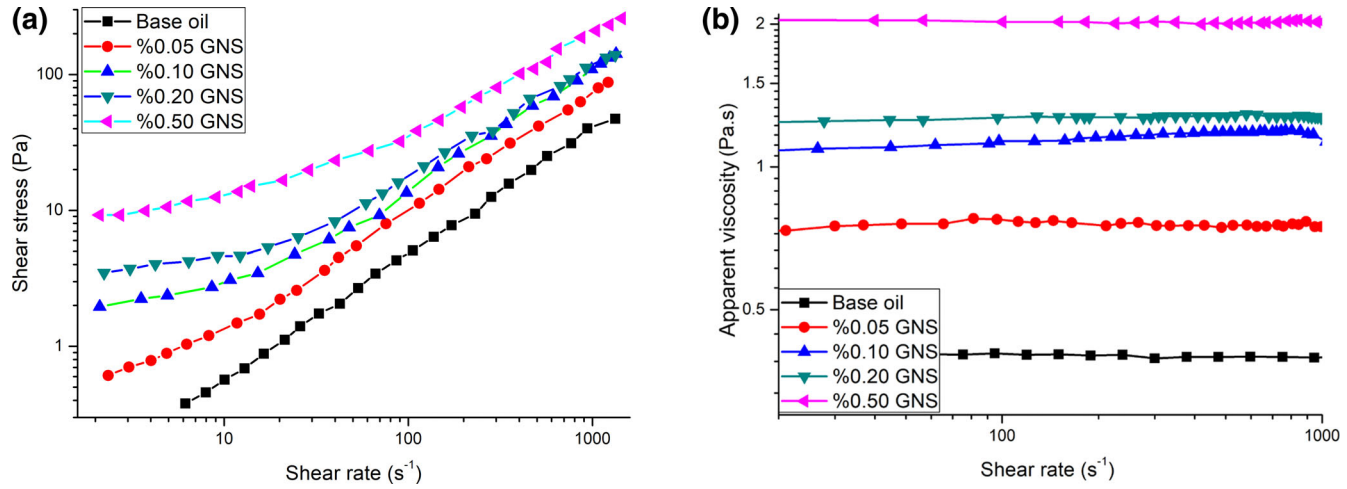

FIGURE 2 (a) Shear stress versus shear rate at 25°C of oil nanofluids containing 0.05–0.5% SilB-graphene oxide (GO) by mass, (b) apparent viscosity versus shear rate. Figures are representatives of produced nanomaterials, for demonstration purposes [Color figure can be viewed at wileyonlinelibrary.com]

TABLE 1 Change of apparent viscosity by temperature

Nanofluid	μ_o	A	t_o	R^2
Base oil	0.0504	2.8991	13.2034	.76
SilA-GNS	0.0744	4.7846	14.7470	.94
SilB-GNS	0.0448	5.4274	15.2393	.99
SilC-GNS	0.3434	7.0898	15.6977	.99

Abbreviation: GNS, graphene nanosheet.

negative slope observed in these graphs arise due to stick–slip interactions or meniscus bridges of liquid films at the sliding interface (Gnecco et al., 2004; Riedo, Gnecco, Bennewitz, Meyer, & Brune, 2003; Tambe & Bhushan, 2005b; Tambe & Bhushan, 2008). As seen in Figure 3, the dominant friction mechanism for SilA-GNS and SilB-GNS, which contain the amine functional group, was the atomic scale stick–slip behavior at both 0.1% and 0.5% concentration and low sliding speeds. This behavior has led to an increase in friction force up to 50 μm/s. The speed dependence of the friction force decreased after 50 μm/s which can occur due to fewer meniscus bridges in the interface, with increasing speed (Tambe & Bhushan, 2005). Also, increasing the friction force with increasing concentration showed that the dominant friction mechanism is viscous forces at the application speeds and loads studied in the analysis. As the meniscus formation decreases with the sliding speed, after about 100 μm/s, the contribution of meniscus formation to friction has weakened. It can be said that nanofluids with nanoparticles added at low concentrations do not behave differently than base oil, and still the dominant mechanism is capillary forces, especially at shear rates of 100 μm/s and above. Furthermore, although the behavior obtained for SilC-GNS showed similarities to others at low concentrations, a change of behavior was observed in friction maps at a concentration of 0.5% by mass.

The horizontal contour lines obtained show that the friction force is not related to sliding speed. Horizontal contour lines emerged at speeds higher than about 80–90 μm/s for nanofluid containing 0.5% SilA-GNS and SilB-GNS, and rather at low speeds (<10 μm/s) for SilC. In studies related to the change of friction force in the nanoscale depending on the speed, it was observed that the friction force is constant with the sliding speed at the speeds where the stick–slip behavior loses its dominance (Gnecco et al., 2004; Riedo et al., 2003). For SilA-GNS and SilB-GNS, the situation that occurs at low concentrations and observed as inclined contour lines were also observed at high nanoparticle concentration. With the increase of sliding speed, both dominant capillary forces and stick–slip forces decreased and the friction force became independent from the sliding speed. This situation occurred in SilC-GNS at low sliding speeds and may have occurred as a result of layer deposition on the surface. Due to the limitations imposed by the scanning speed of the AFM device, the inability to investigate the tribological behavior at higher speeds (especially for SilC-GNS) could not help explain the transition to negative sloping contour lines at high sliding speeds and high normal forces. To determine the friction behavior between the friction pairs with the third component effect of SilC-GNS, FFM tribological analysis was also performed only on the SilC-GNS applied to the surface. Although the repeatability is low due to the layer thicknesses, the results showed that there is a change in friction force independent of the shear rate at low shear rates. The slight negative slope observed at speeds between 20 and 100 μm/s was probably due to the lack of slip-adhesion behavior as the dominant mechanism. This has shown that the friction behavior of SilC-GNS fluids at low sliding speeds behaves independently of speed due to the accumulation of particles on the surface.

3.5 | Wear tests with AFM

The anti-wear properties of different lubricants have been tested on the Si (100) surface. For this purpose, first, trials were carried out

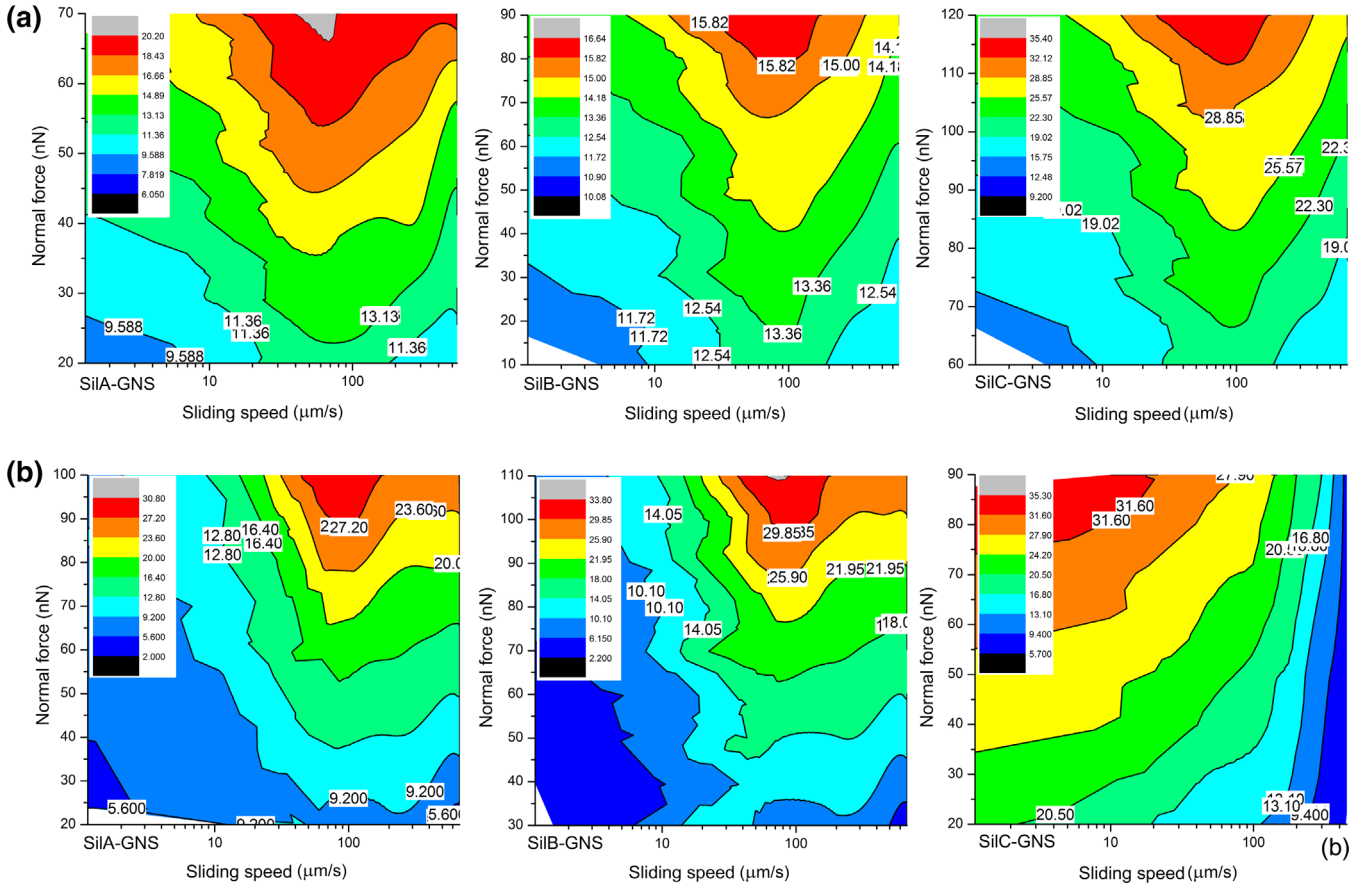

FIGURE 3 Friction maps obtained with oil-based nanofluids containing 0.1% by mass (a) and 0.5% by mass (b) graphene nanosheet (GNS). The friction force is reported as nN [Color figure can be viewed at wileyonlinelibrary.com]

without any lubricants and unfortunately, no significant wear marks were obtained. In the literature, the threshold value reported by Tambe and Bhushan is 2.5 mm/s shear rate, >2 μN normal load, and 250 shear cycles (Ruan & Bhushan, 1994; Tambe & Bhushan, 2005b). This value is well above our AFM device in terms of both scanning speed and normal load. No significant wear traces were found both in the absence of lubricants and in the case of using nanofluids. For this reason, the anti-wear feature was determined by the experiment performed with the ball-on-disc test device. Detailed information about modeling AFM tip using calibration grid and tip deformation is given in Supplementary Document.

3.6 | Thermal conductivity coefficients

Thermal conductivity values determined by measurements at different temperatures using base oil, SilA-GNS, SilB-GNS, and SilC-GNS nanofluids are given in Figure 4. It is seen that the thermal conductivity of nanofluids is higher than the base-oil. This is expected due to the thermal conductivity of the solid particle added to the base oil. Also, an increase in thermal conductivity was observed with an exponential behavior depending not only on the GNS concentration but also on the temperature. The researchers have stated that the increase in thermal conductivity in nanofluids with the Brownian motion of the nanoparticles and the micro convection created by this motion increase the thermal conductivity (Kleinstreuer & Feng, 2011; Yu, France, et al., 2008). Therefore, the Brownian motion is the main mechanism for increasing thermal conductivity. If micro convection is not the dominant heat transfer mechanism, the fact that the high surface area generated by the GNS create low resistance percolation paths may explain the increase in thermal conductivity (Baby & Ramaprabhu, 2010; Choi et al., 2001). The maximum thermal conductivity increase obtained in this study was 46% compared to a base oil (Table 3).

3.7 | Rheological tests with PCM

Since phase shift is very sensitive to the interaction between the AFM tip and the sample surface, phase contrast images can provide some information about the material (Haugstad & Jones, 1999; Tamayo & García, 1997). In the PCM technique, the phase shift of the resonance peak affected by the viscous behavior of the material was measured. Two methods can be preferred to correlate rheological data with PCM test results. One of them is to provide calibration with another measurement technique. The more accurate but relatively more

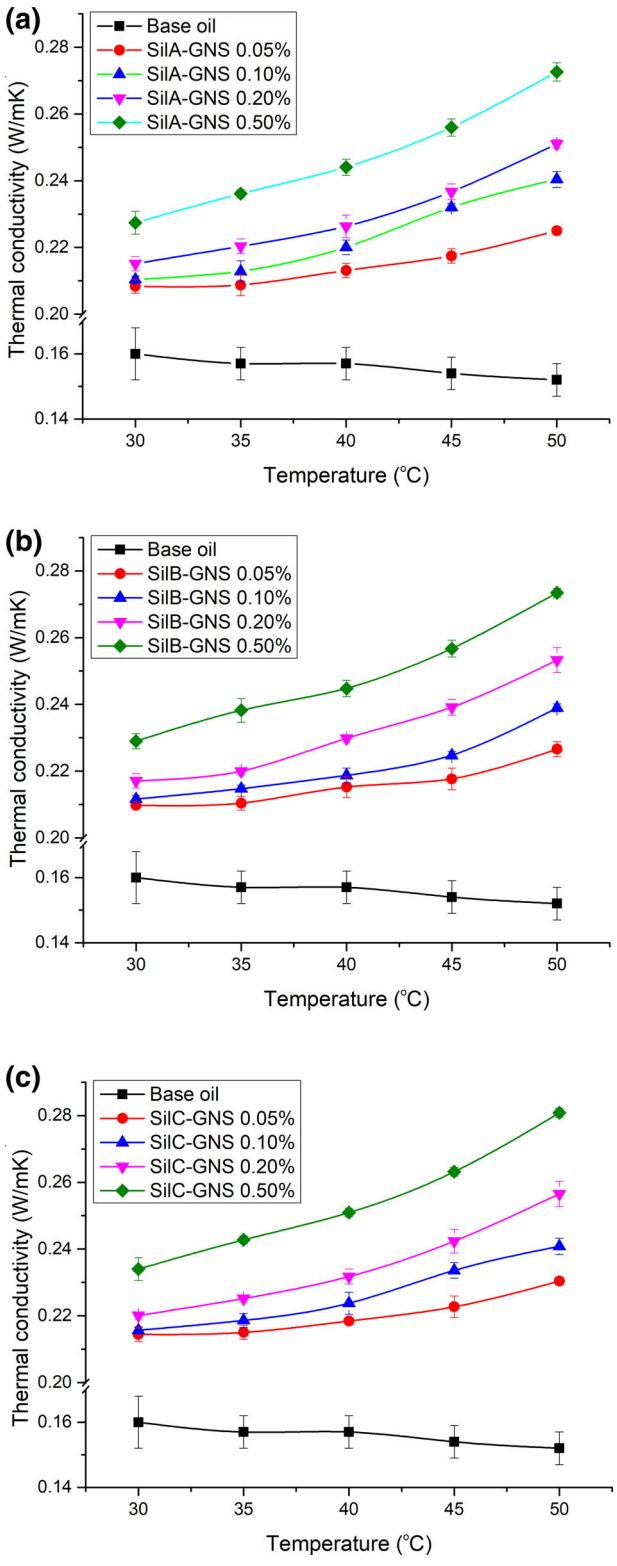

FIGURE 4 Thermal conductivity change at different concentrations and different temperatures for silane-modified nanofluids [Color figure can be viewed at wileyonlinelibrary.com]

difficult one is the modeling and analysis of vibration in noncontact mode (García, Tamayo, & San Paulo, 1999; Scott & Bhushan, 2003). In this study, the calibration technique was used and the relationship between frequency shift viscosity for base oil and nanofluids was 0.0145 ± 0.0004 Pa.s/ phase shift. Viscosity values of nanofluids and base oil obtained with PCM at 25°C are given in Table 2. As can be seen, in the noncontact mode measurements using different setpoints and oscillation frequencies, and by considering the AFM tip interacting only with viscous forces and adhesion force, viscous forces could be measured with PCM. However, repeatability of the measurements was low, possibly due to the nanoparticles adhering to the AFM tip during the oscillation in the nanofluid film. Due to this situation, which is also seen during adhesion measurements, a standard deviation value of around 10% has been achieved. Similar results were obtained when measurements were repeated by calibration using ethylene glycol. However, as a result of calibration using a low viscosity fluid (water), both the standard deviation and the calculated viscosity values were noticeably erroneous.

TABLE 2 Apparent viscosities (Pa.s, 25°C) determined by the PCM technique

GNS% (by weight)	SilA	SilB	SilC
%0.00	0.48 ± 0.02	0.48 ± 0.02	0.48 ± 0.02
%0.05	0.67 ± 0.06	0.78 ± 0.08	0.71 ± 0.7
%0.1	0.96 ± 0.13	1.12 ± 0.07	0.84 ± 0.9
%0.2	1.41 ± 0.09	1.35 ± 0.14	1.21 ± 0.13
%0.5	1.94 ± 0.15	2.01 ± 0.21	1.78 ± 0.17

Abbreviations: GNS, graphene nanosheet; PCM, phase-contrast microscopy.

3.8 | Ball-on-disc tests

Tribological performances of nanofluids were evaluated at 1, 2, and 5 N normal load. The analysis results obtained were smoothed using the 100 points and second-degree polynomial with the Sawatzky–Golay method. Alumina-DIN 18CrMo4 commercial low alloy steel was used as a tribological couple to determine the anti-wear behavior. Alumina has a hardness of 16.14 GPa and is quite high compared to the hardness value of 6.67 GPa given for steel. The results of the tribology tests are summarized in Table 3.

The anti-wear behavior of the nanofluids can be observed after a certain concentration of nanomaterial added in the lubricant. Especially at low concentrations, the wear depth was found close to the value obtained with the base oil. At high concentrations, anti-wear behavior becomes evident. It is known that the anti-abrasion behavior depends not only on the thickness of the film layer formed on the material but also on the nanoparticles that accumulate on the surface. In this case, the anti-wear behavior may have resulted from both the film thickness and the nanosheets accumulating as a layer on the surface and preventing direct contact of tribological pairs. Since the rotation speed (i.e., sliding speed) cannot be changed in the device used, the relationship between sliding speed and friction force was not investigated. The average of the friction coefficient values obtained in

TABLE 3 Tribological test results (5 N normal load, 1,800 s) as wear scar depth (μm) and CoF at a concentration of 0.5% GNS. Also, the increase in the heat transfer coefficient of silane-modified GNS at different concentrations is given in this table

Concentration		0%	0.05%	0.1%	0.2%	0.5%
SilA-GNS	Wear (μm)	2.3 ± 0.4	2.3 ± 0.5	2.2 ± 0.3	1.4 ± 0.3	0.7 ± 0.2
	CoF	0.462 ± 0.040	0.449 ± 0.027	0.417 ± 0.027	0.382 ± 0.015	0.329 ± 0.019
	k%	—	0.30	0.31	0.34	0.42
SilB-GNS	Wear (μm)	2.3 ± 0.4	2.4 ± 0.4	2.0 ± 0.3	1.0 ± 0.3	0.4 ± 0.2
	CoF	0.462 ± 0.040	0.375 ± 0.075	0.340 ± 0.048	0.286 ± 0.057	0.240 ± 0.053
	k%	—	0.31	0.32	0.36	0.43
SilC-GNS	Wear (μm)	2.3 ± 0.4	2.4 ± 0.5	2.0 ± 0.4	0.9 ± 0.3	0.2 ± 0.1
	CoF	0.462 ± 0.040	0.387 ± 0.028	0.375 ± 0.035	0.373 ± 0.031	0.367 ± 0.035
	k%	—	0.34	0.35	0.38	0.46

Abbreviations: CoF, friction coefficient; GNS, graphene nanosheet.

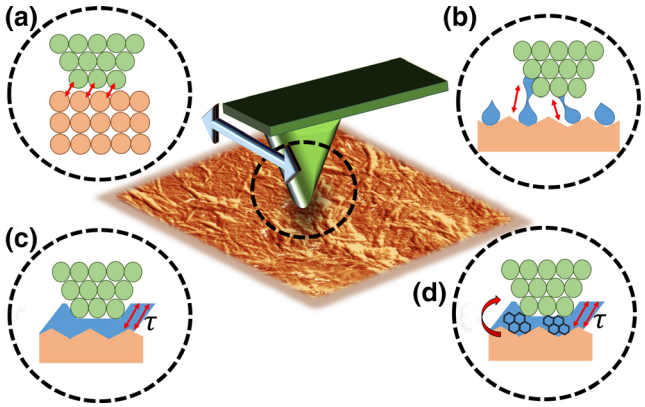

FIGURE 5 The dominant mechanisms in the normal load and sliding speed range used in this study: (a) stick–slip, (b) capillary forces, (c) viscous forces, and (d) load-bearing and rolling [Color figure can be viewed at wileyonlinelibrary.com]

all of the tests was compared with the standard deviation values in Table 3. With 0.5% SilC-GNS nanofluid, antifriction performance is improved by around 44% compared to the base oil. It was determined that the friction coefficient decreases as the concentration of silane-modified GNS in nanofluid increases. Base oil tends to form a thin film between rubbing surfaces, then in the case of base oil containing nanoparticles, nanoparticles can accumulate on rubbing surfaces (Winer, 1967; Xue, Wang, Wen, Wang, & Wang, 2019). In the nanofluid with low nanoparticle concentration, the amount of nanoparticle accumulated on the surface is not sufficient to reduce friction (Wan, Jin, Sun, & Ding, 2015) In this study, as the particle concentration in the nanofluid increased, the roughness on the friction surfaces was effectively filled with accumulated nanoparticles, causing the friction coefficient to decrease. Similar results were obtained by Lu, but in this study, the authors suggested that the rolling effects of spherical nanoparticles caused this reduction (Lu et al., 2007). Various mechanisms have been proposed related to the positive effect of nanoparticles on friction and wear resistance. There are mechanisms such as film formation due to particle accumulation, acting as a ball bearing between the contact surfaces, and forming patches on the surface (Liu et al., 2004; Ou et al., 2010; Xue et al., 2019). As a result, the nanofluids were used successfully as both antifriction and anti-wear lubricants as a base oil substitute.

4 | CONCLUSION

In studies performed using graphene material, the stability of the nanofluid is the main problem. Therefore, in this study, GNSs were modified using 3-aminopropyl triethoxysilane, N-(6-amino hexyl) amino methyl trimethoxysilane and triethoxy (octyl) silane, and oil-based nanofluid was produced with these nanomaterials. It was determined that modified GNSs show higher stability in oil than GO. Besides, the tribological and rheological characterizations of this nanofluidics were performed by scanning probe microscopy. In tribological characterizations, although the load applied in AFM tests is barely sufficient, the dominant mechanisms were atomic (or molecular) stick–slip, meniscus bridges (capillary forces), and viscous fluid-film sliding. Some mechanisms are general in this matter and have been confirmed in the presented study. In Figure 5, predominant friction and wear mechanisms are shown schematically when low sliding speed and/or normal load is applied with FFM.

In the macrotribological examination, the normal load used is relatively high, and plastic deformation has occurred with a sufficient shear rate. In the tribological performance evaluation, the dominant mechanism of lubrication and anti-wear was found as fluid film slip. In the study, graphene-based nanosheets were produced, which were successfully modified with silane molecules. Despite the long production phase, the high stability of the products obtained in the base oil will ensure that these nanomaterials can be used in oil-based lubricants.

Another result obtained from the study is that graphene sheets, which are ruptured and lost their initial shape during the modification processes, have been determined to be successful in terms of viscosity, thermal conductivity, nanofluid stability, and tribological performance. The nanofluids produced in this study showed some shear-

thinning behavior. Moreover, the thermal conductivity of nanofluids increased by around 40%. This again shows that the synthesized nanofluidics will achieve sufficient performance in lubricant applications.

Consequently, mapping of the friction behavior of the material with FFM has shown that this technique is applicable for many different materials. In this study, although the scanning probe techniques have some limitations, it has been shown that the tribological and rheological characterization of a material can be performed using these techniques. It has also been proved that graphene nanomaterials modified with different silane molecules can be successfully used as a nanofluids component for lubricant purposes.

ACKNOWLEDGMENTS

This study was supported by the Scientific and Technical Research Council of Turkey (TUBITAK). The studies within the scope of the project 113M302 were carried out between 2013 and 2015 under the direction of the author, who is a faculty member of the Cumhuriyet University Nanotechnology Engineering Department. The author kindly appreciated that precious financial support by the TÜBİTAK (The Scientific and Technological Research Council of Turkey) (grant number 113M302).

DATA AVAILABILITY STATEMENT

The data that support the findings of this study are available in the Supplementary section, but further information on findings will be available from the corresponding author upon reasonable request.

ORCID

Mustafa Oguzhan Caglayan https://orcid.org/0000-0002-7265-1094

REFERENCES

Ahn, H. S., Chizhik, S. A., Dubravin, A. M., Kazachenko, V. P., & Popov, V. V. (2001). Application of phase contrast imaging atomic force microscopy to tribofilms on DLC coatings. *Wear*, *249*(7), 617–625. https://doi.org/10.1016/S0043-1648(01)00694-9

An Wong, C. H., & Pumera, M. (2014). Highly conductive graphene nanoribbons from the reduction of graphene oxide nanoribbons with lithium aluminium hydride. *Journal of Materials Chemistry C*, *2*(5), 856–863. https://doi.org/10.1039/C3TC31688B

Anczykowski, B., Gotsmann, B., Fuchs, H., Cleveland, J. P., & Elings, V. B. (1999). How to measure energy dissipation in dynamic mode atomic force microscopy. *Applied Surface Science*, *140*(3), 376–382. https://doi.org/10.1016/S0169-4332(98)00558-3

Aravind, S. S. J., Baby, T. T., Arockiadoss, T., Rakhi, R. B., & Ramaprabhu, S. (2011). A cholesterol biosensor based on gold nanoparticles decorated functionalized graphene nanoplatelets. *Thin Solid Films*, *519*(16), 5667–5672. https://doi.org/10.1016/j.tsf.2011.03.032

Baby, T. T., & Ramaprabhu, S. (2010). Investigation of thermal and electrical conductivity of graphene based nanofluids. *Journal of Applied Physics*, *108*(12), 124308. https://doi.org/10.1063/1.3516289

Bahadır, E. B., & Sezgintürk, M. K. (2016). Applications of graphene in electrochemical sensing and biosensing. *TrAC Trends in Analytical Chemistry*, *76*, 1–14. https://doi.org/10.1016/j.trac.2015.07.008

Bar, G., Delineau, L., Brandsch, R., Bruch, M., & Whangbo, M.-H. (1999). Importance of the indentation depth in tapping-mode atomic force microscopy study of compliant materials. *Applied Physics Letters*, *75*(26), 4198–4200. https://doi.org/10.1063/1.125581

Bhushan, B. (2001). Nano- to microscale wear and mechanical characterization using scanning probe microscopy. *Wear*, *251*(1), 1105–1123. https://doi.org/10.1016/S0043-1648(01)00804-3

Bhushan, B., & Kwak, K. J. (2007a). Platinum-coated probes sliding at up to 100 mm s−1against coated silicon wafers for AFM probe-based recording technology. *Nanotechnology*, *18*(34), 345504. https://doi.org/10.1088/0957-4484/18/34/345504

Bhushan, B., & Kwak, K. J. (2007b). Velocity dependence of nanoscale wear in atomic force microscopy. *Applied Physics Letters*, *91*(16), 163113. https://doi.org/10.1063/1.2800375

Bhushan, B., & Ruan, J.-A. (1994). Atomic-scale friction measurements using friction force microscopy: Part II—Application to magnetic media. *Journal of Tribology*, *116*(2), 389–396. https://doi.org/10.1115/1.2927241

Binggeli, M., & Mate, C. M. (1994). Influence of capillary condensation of water on nanotribology studied by force microscopy. *Applied Physics Letters*, *65*(4), 415–417. https://doi.org/10.1063/1.113020

Chang, L., Zhang, Z., Zhang, H., & Friedrich, K. (2005). Effect of nanoparticles on the tribological behaviour of short carbon fibre reinforced poly(etherimide) composites. *Tribology International*, *38*(11), 966–973. https://doi.org/10.1016/j.triboint.2005.07.026

Charrier, A., & Thibaudau, F. (2005). Main phase transitions in supported lipid single-bilayer. *Biophysical Journal*, *89*(2), 1094–1101. https://doi.org/10.1529/biophysj.105.062463

Chen, J.-H., Ishigami, M., Jang, C., Hines, D. R., Fuhrer, M. S., & Williams, E. D. (2007). Printed graphene circuits. *Advanced Materials*, *19*(21), 3623–3627. https://doi.org/10.1002/adma.200701059

Chen, S., Liu, W., & Yu, L. (1998). Preparation of DDP-coated PbS nanoparticles and investigation of the antiwear ability of the prepared nanoparticles as additive in liquid paraffin. *Wear*, *218*(2), 153–158. https://doi.org/10.1016/S0043-1648(98)00220-8

Childs, T. H. C. (1983). Fine friction cutting: A useful wear process. *Tribology International*, *16*(2), 67–84. https://doi.org/10.1016/0301-679X(83)90018-X

Choi, S. U. S., & Eastman, J. Oak Ridge, TN, USA: U.S. Department of Energy Office of Scientific and Technical Information; (1995). *Enhancing thermal conductivity of fluids with nanoparticles*. ASME International Mechanical Engineering Congress & Exposition, November 12-17 1995, San Fransisco, USA (Vol. 66). https://www.osti.gov/servlets/purl/196525.

Choi, S. U. S., Zhang, Z. G., Yu, W., Lockwood, F. E., & Grulke, E. A. (2001). Anomalous thermal conductivity enhancement in nanotube suspensions. *Applied Physics Letters*, *79*(14), 2252–2254. https://doi.org/10.1063/1.1408272

Choi, Y., Lee, C., Hwang, Y., Park, M., Lee, J., Choi, C., & Jung, M. (2009). Tribological behavior of copper nanoparticles as additives in oil. *Current Applied Physics*, *9*(Suppl 2), e124–e127. https://doi.org/10.1016/j.cap.2008.12.050

Eastman, J. A., Choi, S. U. S., Li, S., Yu, W., & Thompson, L. J. (2001). Anomalously increased effective thermal conductivities of ethylene glycol-based nanofluids containing copper nanoparticles. *Applied Physics Letters*, *78*(6), 718–720. https://doi.org/10.1063/1.1341218

Eswaraiah, V., Sankaranarayanan, V., & Ramaprabhu, S. (2011a). Functionalized graphene–PVDF foam composites for EMI shielding. *Macromolecular Materials and Engineering*, *296*(10), 894–898. https://doi.org/10.1002/mame.201100035

Eswaraiah, V., Sankaranarayanan, V., & Ramaprabhu, S. (2011b). Graphene-based engine oil nanofluids for tribological applications. *ACS Applied Materials & Interfaces*, *3*(11), 4221–4227. https://doi.org/10.1021/am200851z

Gao, Y., Sun, R., Zhang, Z., & Xue, Q. (2000). Tribological properties of oleic acid—Modified TiO2 nanoparticle in water. *Materials Science and*

Engineering A, *286*(1), 149–151. https://doi.org/10.1016/S0921-5093(00)00626-2

Gara, L., & Zou, Q. (2012). Friction and wear characteristics of water-based ZnO and Al2O3 nanofluids. *Tribology Transactions*, *55*(3), 345–350. https://doi.org/10.1080/10402004.2012.656879

Gara, L., & Zou, Q. (2013). Friction and wear characteristics of oil-based ZnO nanofluids. *Tribology Transactions*, *56*(2), 236–244. https://doi.org/10.1080/10402004.2012.740148

García, R., Tamayo, J., & San Paulo, A. (1999). Phase contrast and surface energy hysteresis in tapping mode scanning force microscopy. *Surface and Interface Analysis*, *27*(5), 312–316. https://doi.org/10.1002/(SICI)1096-9918(199905/06)27:5/6<312::AID-SIA496>3.0.CO;2-Y

Ghadimi, A., Saidur, R., & Metselaar, H. S. C. (2011). A review of nanofluid stability properties and characterization in stationary conditions. *International Journal of Heat and Mass Transfer*, *54*(17), 4051–4068. https://doi.org/10.1016/j.ijheatmasstransfer.2011.04.014

Gnecco, E., Bennewitz, R., Pfeiffer, O., Socoliuc, A., & Meyer, E. (2004). Friction and wear on the atomic scale. In B. Bhushan (Ed.), *Springer handbook of nanotechnology* (pp. 631–660). Berlin: Springer Berlin Heidelberg.

Gu, C., Li, Q., Gu, Z., & Zhu, G. (2008). Study on application of CeO2 and CaCO3 nanoparticles in lubricating oils. *Journal of Rare Earths*, *26*(2), 163–167. https://doi.org/10.1016/S1002-0721(08)60058-7

Haugstad, G., & Jones, R. R. (1999). Mechanisms of dynamic force microscopy on polyvinyl alcohol: Region- specific non-contact and intermittent contact regimes. *Ultramicroscopy*, *76*(1–2), 77–86. https://doi.org/10.1016/S0304-3991(98)00073-4

He, Y., Jin, Y., Chen, H., Ding, Y., Cang, D., & Lu, H. (2007). Heat transfer and flow behaviour of aqueous suspensions of TiO2 nanoparticles (nanofluids) flowing upward through a vertical pipe. *International Journal of Heat and Mass Transfer*, *50*(11), 2272–2281. https://doi.org/10.1016/j.ijheatmasstransfer.2006.10.024

Hernandez Battez, A., Fernandez Rico, J. E., Navas Arias, A., Viesca Rodriguez, J. L., Chou Rodriguez, R., & Diaz Fernandez, J. M. (2006). The tribological behaviour of ZnO nanoparticles as an additive to PAO6. *Wear*, *261*(3–4), 256–263. https://doi.org/10.1016/j.wear.2005.10.001

Hernández Battez, A., González, R., Viesca, J. L., Fernández, J. E., Díaz Fernández, J. M., Machado, A., … Riba, J. (2008). CuO, ZrO2 and ZnO nanoparticles as antiwear additive in oil lubricants. *Wear*, *265*(3–4), 422–428. https://doi.org/10.1016/j.wear.2007.11.013

Hsu, J. H., & Chang, S. H. (2009). Tribological interaction between multi-walled carbon nanotubes and silica surface using lateral force microscopy. *Wear*, *266*(9–10), 952–959. https://doi.org/10.1016/j.wear.2008.12.017

Hu, Z. S., & Dong, J. X. (1998). Study on antiwear and reducing friction additive of nanometer titanium oxide. *Wear*, *216*(1), 92–96. https://doi.org/10.1016/S0043-1648(97)00252-4

Hu, Z. S., Dong, J. X., & Chen, G. X. (1998). Study on antiwear and reducing friction additive of nanometer ferric oxide. *Tribology International*, *31*(7), 355–360. https://doi.org/10.1016/S0301-679X(98)00042-5

Hummers, W. S., & Offeman, R. E. (1958). Preparation of graphitic oxide. *Journal of the American Chemical Society*, *80*(6), 1339–1339. https://doi.org/10.1021/ja01539a017

Hwang, Y., Lee, C., Choi, Y., Cheong, S., Kim, D., Lee, K., … Kim, S. H. (2011). Effect of the size and morphology of particles dispersed in nano-oil on friction performance between rotating discs. *Journal of Mechanical Science and Technology*, *25*(11), 2853–2857. https://doi.org/10.1007/s12206-011-0724-1

James, P. J., Antognozzi, M., Tamayo, J., McMaster, T. J., Newton, J. M., & Miles, M. J. (2001). Interpretation of contrast in tapping mode AFM and shear force microscopy. A study of Nafion. *Langmuir*, *17*(2), 349–360. https://doi.org/10.1021/la000332h

Jiao, D., Zheng, S., Wang, Y., Guan, R., & Cao, B. (2011). The tribology properties of alumina/silica composite nanoparticles as lubricant additives. *Applied Surface Science*, *257*(13), 5720–5725. https://doi.org/10.1016/j.apsusc.2011.01.084

Kao, M. J., & Lin, C. R. (2009). Evaluating the role of spherical titanium oxide nanoparticles in reducing friction between two pieces of cast iron. *Journal of Alloys and Compounds*, *483*(1–2), 456–459. https://doi.org/10.1016/j.jallcom.2008.07.223

Kleinstreuer, C., & Feng, Y. (2011). Experimental and theoretical studies of nanofluid thermal conductivity enhancement: A review. *Nanoscale Research Letters*, *6*(1), 229. https://doi.org/10.1186/1556-276X-6-229

Kumar, A., Reddy, A. L. M., Mukherjee, A., Dubey, M., Zhan, X., Singh, N., … Ajayan, P. M. (2011). Direct synthesis of lithium-intercalated graphene for electrochemical energy storage application. *ACS Nano*, *5*(6), 4345–4349. https://doi.org/10.1021/nn201527p

Lee, C., Wei, X., Kysar, J. W., & Hone, J. (2008). Measurement of the elastic properties and intrinsic strength of monolayer graphene. *Science*, *321*(5887), 385–388. https://doi.org/10.1126/science.1157996

Lee, J. W., Ko, J. M., & Kim, J.-D. (2012). Hydrothermal preparation of nitrogen-doped graphene sheets via hexamethylenetetramine for application as supercapacitor electrodes. *Electrochimica Acta*, *85*, 459–466. https://doi.org/10.1016/j.electacta.2012.08.070

Li, J., Xie, H. Q., Li, Y., Liu, J., & Li, Z. X. (2011). Electrochemical properties of graphene nanosheets/polyaniline nanofibers composites as electrode for supercapacitors. *Journal of Power Sources*, *196*(24), 10775–10781. https://doi.org/10.1016/j.jpowsour.2011.08.105

Liu, G., Li, X., Qin, B., Xing, D., Guo, Y., & Fan, R. (2004). Investigation of the mending effect and mechanism of copper nano-particles on a tribologically stressed surface. *Tribology Letters*, *17*(4), 961–966. https://doi.org/10.1007/s11249-004-8109-6

Liu, H., & Bhushan, B. (2003). Nanotribological characterization of molecularly thick lubricant films for applications to MEMS/NEMS by AFM. *Ultramicroscopy*, *97*(1–4), 321–340. https://doi.org/10.1016/S0304-3991(03)00058-5

Lotya, M., King, P. J., Khan, U., De, S., & Coleman, J. N. (2010). High-concentration, surfactant-stabilized graphene dispersions. *ACS Nano*, *4*(6), 3155–3162. https://doi.org/10.1021/nn1005304

Lu, H. F., Fei, B., Xin, J. H., Wang, R. H., Li, L., & Guan, W. C. (2007). Synthesis and lubricating performance of a carbon nanotube seeded miniemulsion. *Carbon*, *45*(5), 936–942. https://doi.org/10.1016/j.carbon.2007.01.001

Maivald, P., Butt, H. J., Gould, S. A. C., Prater, C. B., Drake, B., Gurley, J. A., … Hansma, P. K. (1991). Using force modulation to image surface elasticities with the atomic force microscope. *Nanotechnology*, *2*(2), 103–106. https://doi.org/10.1088/0957-4484/2/2/004

Marconnet, A. M., Panzer, M. A., & Goodson, K. E. (2013). Thermal conduction phenomena in carbon nanotubes and related nanostructured materials. *Reviews of Modern Physics*, *85*(3), 1295–1326. https://doi.org/10.1103/RevModPhys.85.1295

Marti, O. (1993). Friction and measurement of friction on a nanometer scale. *Surface and Coatings Technology*, *62*(1–3), 510–516. https://doi.org/10.1016/0257-8972(93)90292-V

Moser, A. E., & Eckhardt, C. J. (2001). Method for reliable measurement of relative frictional properties of different self-assembled monolayers using frictional force microscopy. *Thin Solid Films*, *382*(1–2), 202–213. https://doi.org/10.1016/S0040-6090(00)01681-3

Nika, D. L., Pokatilov, E. P., Askerov, A. S., & Balandin, A. A. (2009). Phonon thermal conduction in graphene: Role of Umklapp and edge roughness scattering. *Physical Review B*, *79*(15), 155413. https://doi.org/10.1103/PhysRevB.79.155413

Novoselov, K. S., Geim, A. K., Morozov, S. V., Jiang, D., Zhang, Y., Dubonos, S. V., … Firsov, A. A. (2004). Electric field effect in atomically thin carbon films. *Science*, *306*(5696), 666–669. https://doi.org/10.1126/science.1102896

Ogletree, D. F., Carpick, R. W., & Salmeron, M. (1996). Calibration of frictional forces in atomic force microscopy. *Review of Scientific Instruments*, *67*(9), 3298–3306. https://doi.org/10.1063/1.1147411

Ou, J., Wang, J., Liu, S., Mu, B., Ren, J., Wang, H., & Yang, S. (2010). Tribology study of reduced graphene oxide sheets on silicon substrate synthesized via covalent assembly. *Langmuir*, *26*(20), 15830–15836. https://doi.org/10.1021/la102862d

Park, S., & Ruoff, R. S. (2009). Chemical methods for the production of graphenes. *Nature Nanotechnology*, *4*(4), 217–224. https://doi.org/10.1038/nnano.2009.58

Peñas, J. R. V., Zárate, J. M. O. d., & Khayet, M. (2008). Measurement of the thermal conductivity of nanofluids by the multicurrent hot-wire method. *Journal of Applied Physics*, *104*(4), 044314. https://doi.org/10.1063/1.2970086

Peng, D. X., Chen, C. H., Kang, Y., Chang, Y. P., & Chang, S. Y. (2010). Size effects of SiO2 nanoparticles as oil additives on tribology of lubricant. *Industrial Lubrication and Tribology*, *62*(2), 111–120. https://doi.org/10.1108/00368791011025656

Qu, L., Liu, Y., Baek, J.-B., & Dai, L. (2010). Nitrogen-doped graphene as efficient metal-free electrocatalyst for oxygen reduction in fuel cells. *ACS Nano*, *4*(3), 1321–1326. https://doi.org/10.1021/nn901850u

Reeves, C. J., Menezes, P. L., Lovell, M. R., & Jen, T. C. (2013). The size effect of boron nitride particles on the tribological performance of biolubricants for energy conservation and sustainability. *Tribology Letters*, *51*(3), 437–452. https://doi.org/10.1007/s11249-013-0182-2

Reinstädtler, M., Rabe, U., Goldade, A., Bhushan, B., & Arnold, W. (2005). Investigating ultra-thin lubricant layers using resonant friction force microscopy. *Tribology International*, *38*(6), 533–541. https://doi.org/10.1016/j.triboint.2005.01.022

Riedo, E., Gnecco, E., Bennewitz, R., Meyer, E., & Brune, H. (2003). Interaction potential and hopping dynamics governing sliding friction. *Physical Review Letters*, *91*(8):084502/1–084502/4. https://doi.org/10.1103/PhysRevLett.91.084502

Ruan, J. A., & Bhushan, B. (1994). Atomic-scale friction measurements using friction force microscopy: Part I-general principles and new measurement techniques. *Journal of Tribology*, *116*(2), 378–388. https://doi.org/10.1115/1.2927240

Saidur, R., Leong, K. Y., & Mohammed, H. A. (2011). A review on applications and challenges of nanofluids. *Renewable and Sustainable Energy Reviews*, *15*(3), 1646–1668. https://doi.org/10.1016/j.rser.2010.11.035

Schniepp, H. C., Li, J. L., McAllister, M. J., Sai, H., Herrera-Alonson, M., Adamson, D. H., … Aksay, I. A. (2006). Functionalized single graphene sheets derived from splitting graphite oxide. *Journal of Physical Chemistry B*, *110*(17), 8535–8539. https://doi.org/10.1021/jp060936f

Scott, W. W., & Bhushan, B. (2003). Use of phase imaging in atomic force microscopy for measurement of viscoelastic contrast in polymer nanocomposites and molecularly thick lubricant films. *Ultramicroscopy*, *97*(1–4), 151–169. https://doi.org/10.1016/S0304-3991(03)00040-8

Stachowiak, G. W., & Batchelor, A. W. (2006). Introduction. In G. W. Stachowiak & A. W. Batchelor (Eds.), *Engineering tribology (third edition)* (pp. 1–9). Burlington, VT: Butterworth-Heinemann.

Stankovich, S., Dikin, D. A., Piner, R. D., Kohlhaas, K. A., Kleinhammes, A., Jia, Y., … Ruoff, R. S. (2007). Synthesis of graphene-based nanosheets via chemical reduction of exfoliated graphite oxide. *Carbon*, *45*(7), 1558–1565. https://doi.org/10.1016/j.carbon.2007.02.034

Ţălu, Ş. 1. Cluj-Napoca Romania: Napoca Star Publishing House; (2015). In *Micro and nanoscale characterization of three-dimensional surfaces: Basics and Applications*. 64–72.

Tamayo, J., & García, R. (1997). Effects of elastic and inelastic interactions on phase contrast images in tapping-mode scanning force microscopy. *Applied Physics Letters*, *71*(16), 2394–2396. https://doi.org/10.1063/1.120039

Tambe, N. S., & Bhushan, B. (2004). Scale dependence of micro/nano-friction and adhesion of MEMS/NEMS materials, coatings and lubricants. *Nanotechnology*, *15*(11), 1561–1570. https://doi.org/10.1088/0957-4484/15/11/033

Tambe, N. S., & Bhushan, B. (2005). Identifying materials with low friction and adhesion for nanotechnology applications. *Applied Physics Letters*, *86*(6), 061906. https://doi.org/10.1063/1.1856688

Tambe, N. S., & Bhushan, B. (2005a). Friction model for the velocity dependence of nanoscale friction. *Nanotechnology*, *16*(10), 2309–2324. https://doi.org/10.1088/0957-4484/16/10/054

Tambe, N. S., & Bhushan, B. (2005b). Nanowear mapping: A novel atomic force microscopy based approach for studying nanoscale wear at high sliding velocities. *Tribology Letters*, *20*(1), 83–90. https://doi.org/10.1007/s11249-005-7795-z

Tambe, N. S., & Bhushan, B. (2008). Nanoscale friction and wear maps. *Philosophical Transactions of the Royal Society A: Mathematical, Physical and Engineering Sciences*, *366*(1869), 1405–1424. https://doi.org/10.1098/rsta.2007.2165

Tao, Z., & Bhushan, B. (2006). New technique for studying nanoscale friction at sliding velocities up to 200mm/s using atomic force microscope. *Review of Scientific Instruments*, *77*(10), 103705. https://doi.org/10.1063/1.2358690

Tao, Z., & Bhushan, B. (2007). Velocity dependence and rest time effect on nanoscale friction of ultrathin films at high sliding velocities. *Journal of Vacuum Science and Technology A: Vacuum, Surfaces and Films*, *25*(4), 1267–1274. https://doi.org/10.1116/1.2435381

Wan, Q., Jin, Y., Sun, P., & Ding, Y. (2015). Tribological behaviour of a lubricant oil containing boron nitride nanoparticles. *Procedia Engineering*, *102*, 1038–1045. https://doi.org/10.1016/j.proeng.2015.01.226

Winer, W. O. (1967). Molybdenum disulfide as a lubricant: A review of the fundamental knowledge. *Wear*, *10*(6), 422–452. https://doi.org/10.1016/0043-1648(67)90187-1

Wu, Y. Y., Tsui, W. C., & Liu, T. C. (2007). Experimental analysis of tribological properties of lubricating oils with nanoparticle additives. *Wear*, *262*(7–8), 819–825. https://doi.org/10.1016/j.wear.2006.08.021

Wu, Z.-S., Ren, W., Gao, L., Liu, B., Jiang, C., & Cheng, H.-M. (2009). Synthesis of high-quality graphene with a pre-determined number of layers. *Carbon*, *47*(2), 493–499. https://doi.org/10.1016/j.carbon.2008.10.031

Xu, C., Shi, X., Ji, A., Shi, L., Zhou, C., & Cui, Y. (2015). Fabrication and characteristics of reduced graphene oxide produced with different green reductants. *PLoS One*, *10*(12), e0144842. https://doi.org/10.1371/journal.pone.0144842

Xu, P., Yan, X., Cong, P., Zhu, X., & Li, D. (2017). Silane coupling agent grafted graphene oxide and its modification on polybenzoxazine resin. *Composite Interfaces*, *24*(7), 635–648. https://doi.org/10.1080/09276440.2017.1254989

Xue, C., Wang, S., Wen, D., Wang, G., & Wang, Y. (2019). Tribological performance of nanocomposite carbon lubricant additive. *Materials (Basel, Switzerland)*, *12*(1), 149. https://doi.org/10.3390/ma12010149

Yu, H. l., Xu, Y., Shi, P. j., Xu, B. s., Wang, X. l., & Liu, Q. (2008). Tribological properties and lubricating mechanisms of cu nanoparticles in lubricant. *Transactions of Nonferrous Metals Society of China (English Edition)*, *18*(3), 636–641. https://doi.org/10.1016/S1003-6326(08)60111-9

Yu, W., France, D. M., Routbort, J. L., & Choi, S. U. S. (2008). Review and comparison of nanofluid thermal conductivity and heat transfer enhancements. *Heat Transfer Engineering*, *29*(5), 432–460. https://doi.org/10.1080/01457630701850851

Yu, W., & Xie, H. (2012). A review on nanofluids: Preparation, stability mechanisms, and applications. *Journal of Nanomaterials*, *2012*, 1–17. https://doi.org/10.1155/2012/435873

Zhang, W., Zhou, M., Zhu, H., Tian, Y., Wang, K., Wei, J., … Wu, D. (2011). Tribological properties of oleic acid-modified graphene as lubricant oil additives. *Journal of Physics D: Applied Physics*, *44*(20), 205303. https://doi.org/10.1088/0022-3727/44/20/205303

Zhao, C., Chen, Y. K., & Ren, G. (2017). A study of tribological properties of water-based ceria nanofluids. *Tribology and Lubrication Technology*, *73*(3), 56–66.

SUPPORTING INFORMATION

Additional supporting information may be found online in the Supporting Information section at the end of this article.

How to cite this article: Caglayan MO. Rheological and tribological characterization of novel modified graphene/oil-based nanofluids using force microscopy. *Microsc Res Tech*. 2021;84:814–827. https://doi.org/10.1002/jemt.23641